Study of the effects from an oval JWST PSF on the recoverability of the structural parameters of faint galaxies

Rolf A. Jansen, Rogier A. Windhorst, and Seth H. Cohen

Department of Physics and Astronomy, Arizona State University, Box 871504, Tempe, AZ 85287-1504

Email: Rogier.Windhorst@asu.edu

ABSTRACT

We present the preliminary results of an extensive set of simulations designed to study the effect of the shape and size of the JWST Point Spread Function (PSF) on the accuracy with which structural parameters may be recovered for faint and distant galaxies. This study was prompted by the recent discussion of a descope option for JWST where only the central structure of the selected design would be implemented and that would result in a strongly non-circular PSF.

We compare results for round mirrors of 7 and 6 m diameter with those for an elliptical mirror with major and minor axis diameters of 8 and 4 m, concentrating in particular on models of faint galaxies with $m_{AB}(2\mu m) \gtrsim 27.5$ mag.

Our main result is, that for equal mirror surface area, a non-circular aperture does not allow one to recover characteristic radii, ellipticities, and position angles to as faint a magnitude as a circular aperture does, even after convolution with the transposed PSF or Lucy-Richardson deconvolution.

1. Introduction

This study was prompted by the recent discussion of a descope option for JWST where only the central structure of the selected design would be implemented and that would result in a strongly non-circular PSF.

It has been suggested that oval PSF's are not disastrous for faint galaxy studies, since the images can be deconvolved. However, upon further reflection and after detailed simulations, this is not true because of the following reasons:

(1) Optical CCD and IR detector images cannot be deconvolved to arbitrarily faint levels, since a good fraction or most of the image noise is made by the detector (read-noise, dark-current, cosmic rays) and therefore has never gone through the telescope. Hence the image noise, contrary to the image signal, does *not* bear the PSF of the telescope. This is quite contrary to radio interferometers, where one can deconvolve images to well into the noise without penalty of introducing artifacts, since all of the data was made in the UV-plane, including the noise, and so *both* the image noise *and* the image signal bear the PSF of the telescope (Windhorst et al. 1984).

(2) The process of deconvolution has been proven to be mathematically equivalent to a least squares fit to the data in the UV-plane (Schwarz 1978). As a consequence, deconvolution results in some sharpening

of the image FWHM, to the extent that the UV-plane coverage was not symmetric and to the extent that a reasonable extrapolation in the UV-plane is possible. This is commonly believed to not be more than a factor of 2 in spatial frequency, and all deconvolution algorithms as a consequence show a very slow increase in image resolution that roughly scales as FWHM$\propto$S/N$^{-1/8}$ (Gull MEM reference here). Hence, an image object has to have at least $S/N \gtrsim 250$ in order for deconvolution to provide an increase in image resolution of at most a factor 2. For the approximation of an elliptical Gaussian beam, and an intrinsically elliptical Gaussian source, this deconvolution can in principle be done analytically using (small) differences between sin's and cosines (Wild 1970).

(3) Deconvolution of small objects that are barely bigger than the PSF leads to non-linear biases in parameter measurements. These are already present in the case of S/N$\rightarrow \infty$, as discussed in Windhorst et al. (1984), which therefore constitutes a fundamental limitation to the usefulness of any deconvolution technique (Schwarz 1978, Lucy 1974), even the simple ones (Wild 1970).

(4) A more fundamental limitation than the previous three is that the slope of all objects counts is steep ($\alpha \simeq$0.2–0.4), so that almost all objects detected by JWST will be faint. As a consequence, the image noise that did not go through the telescope and so does not bear the telescope PSF will turn deconvolution into a very heavily non-linear algorithm (Windhorst et al. 1984, Condon 1997). This is in addition to the non-linear biases in parameter measurements already present in the case of S/N$\rightarrow \infty$ as discussed in (3).

In summary, deconvolution is not a pretty solution anywhere in astronomy, except for perhaps the case of *interpolation* missing data in the UV-plane as the CLEAN algorithms applied in radio astronomy. However, to get rid of the oval PSF suggested for the JWST, an effective *extrapolation* of the data in the UV-plane is needed, which is subject to all the fundamental uncertainties (1)–(4) above.

An oval PSF will also push JWST closer to the natural confusion limit (Windhorst et al. 2003), which is not desirable in deep–ultradeep JWST images (AB-limits$\gtrsim$31–32 mag). For this reason, we do not consider convolving the oval JWST PSF with another oval PSF that is its conjugate, so that the effective PSF is round but $\sim$2$\times$ large than the original PSF. This would also result in an effective image S/N that differs by $\sim$sqrt(2), leading to the biases already observed in this study.

In conclusion, applying deconvolution algorithms is like having nuclear weapons — their best use is to make sure they will never have to be used ...

2. Strategy

2.1. JWST telescope and instrument parameters

We will consider three configurations for the JWST primary mirror:

(1) the nominal 7 m diameter (approximately) round segmented mirror, as in the TRW design.

(2) the required 6 m diameter round segmented mirror, and

(3) the central portion of the segmented mirror structure with a major axis diameter of 8 m and with a minor axis diameter of 4 m.

Configuration (3) serves as a benchmark model for the descope option that has recently been proposed. If the primary cannot be produced with an major axis diameter in excess of 7 m, then in order to meet the

minimal requirements of a 25 m^2 aperture, the minor axis diameter should be 4.6 m and the axis ratio would be ∼0.66 rather than 0.5. We assume the central hole in the mirror to have a diameter of 0.5625 m.

As our baseline wavelength and instrument for this preliminary study we chose $2\mu m$ and the short wavelength (OPT-ACCUM) channel of NIRCAM. The requirement that JWST be diffraction limited longwards of this wavelength gives us an expected resolution of $0\farcs072$ and $0\farcs084$ for the 7 m and 6 m round primary, respectively, and pixel scales of $0\farcs0386$/pix and $0\farcs0451$/pix, respectively.

In order not to undersample the PSF corresponding to the major axis of an 8×4 m elliptical mirror, we assume a pixel scale of $0\farcs0386$/pix. The InSb detector is assumed to have a Gaussian read noise of 4.41 e^-, dark current of 0.00444 e^-/s, and a gain of 3.5 e^-/DN.

2.2. Adopted Sky Background in L2

We adopt the median background and irradiation environments for JWST in its L2 orbit, and assume a pointing near the Ecliptic North Pole, as modeled for the nominal 7 m telescope using the NGST Mission Simulator (see: *www.ngst.stsci.edu/nms/*). For a median background consisting of zodiacal light (1.80×10^{-1} e^-/s/pix), star light scattered off of the primary and secondary mirrors ($(9.32+6.71)\times10^{-3}$ e^-/s/pix), zodiacal light scattered off of the primary and secondary mirrors ($(3.20+2.05)\times10^{-3}$ e^-/s/pix), and negligible thermal self-emission of telescope and rear of the solar shield structure (at $2\mu m$ and $T = 40$K), we expect a total background of $(0.20128 + 0.00444) = 0.20572$ e^-/s/pix. These rates are scaled in models for apertures other than the nominal one.

2.3. Cosmic rays and exposure times

A realistic cosmic ray flux was modeled in accordance with the study by Rauscher, Isaacs & Long (2000). Also in accordance with their findings we opted to divide our baseline 1 hour exposure into eight relatively short individual exposures of only 450 s each, rather than take fewer but longer exposures (e.g., 4×900 s or 3×1200 s). The latter one might expect to be more suitable, but were shown by Rauscher et al. to lead to larger variations in effective pixel-to-pixel sensitivity of a stacked exposure, and hence larger errors in the surface photometry.

2.4. Galaxy model parameters

We wish to accurately model the faint and distant galaxies and sub-galactic size building blocks expected in deep JWST survey fields (Driver et al. 1995, 1998; Pascarelle et al. 1996, Odewahn et al. 1996, Windhorst et al. 1998, 2002b). The grid of model parameters will reflect this, and in particular a representative coverage of the expected galaxy scale-lengths (measured as half-light radii r_e ; Odewahn et al. 1996) and axis ratios b/a (Odewahn et al. 1997).

We vary r_e between 2.089–10.47 pixels corresponding to linear sizes in the range 0.7–3.7 kpc at $z \simeq 2$ and 0.3–1.6 kpc at $z \simeq 10$ (see: Windhorst, Conselice & Petro 2003, their Fig. 1). The aspect ratio is varied between face-on (and intrinsically round) and edge-on (with intrinsic minimum thickness of 0.1 times the radial extent). Magnitudes were selected initially on an arbitrary instrumental scale between $m* = 26.5$–

31.0 mag. These were later calibrated using the NMS instrument throughput and by scaling from the *HST*/NICMOS Hubble Deep Field zero-points. We adopt a zero-point of $m^{\rm zp}_{AB}(2\mu m) = 28.57$ mag for the nominal 7 m telescope and 28.11 and 28.24 mag for the descoped 8×4 m and 6 m telescopes, respectively, the differences reflecting the difference in effective aperture area. We note that at this point these zero-points are only tentative and do not affect the issue at hand. The model input magnitudes, $m*$, therefore correspond to calibrated magnitudes in the range $m_{AB}(2\mu m) = 27.9$–32.4 mag, as expected for the range of fluxes covered in most JWST images (Windhorst et al. 2002b, 2003).

A complete listing of the model grids used as well as the IRAF script to run the simulations is given in Appendix A.

3. Results

Median trends and quartile (25%–75%) ranges were computed for object simulations for each of the different model parameters and results are presented in the figures in this section. Each data point in these plots represents the median of hundreds of realizations of a given galaxy model (typically 840[1], and less at the faintest magnitudes where some modeled objects were no longer detected). The quartile range of the observed parameters is represented as error bars in Figs. 1–10. That quartile ranges tend to increase at fainter magnitudes is expected, but we are interested here in the relative increase in the quartile range and in offsets between the the different telescope configurations.

3.1. Simulations in real sky-images

To shortcut any of the shortcomings of the artificial sky simulations above, we also did some simulations of real-sky images for JWST.

For this, we started with the original 50-orbit HDF-N F814W image, which is representative for a 5-hr J–K band image with a 7-meter JWST with a round PSF. This ignores effects from the rest-frame wavelength or morphological K-correction, which are to first order small over the sampled redshift range of interest (Windhorst et al. 2002). The results are shown in Fig. 11–13 (panels a). The simulated 5-hr JWST image assumes an oval PSF for a descoped JWST mirror of assumed size 8x4 meters. This image was obtained by convolving the HDF-N images with the appropriate elliptical PSF, which in this case is clearly East-West extended (Fig. 11–13 panels b). This simulated 5-hr JWST image with the oval PSF has lower sky-noise, since convolution smooths the noise. For this reason, Gaussian noise equivalent to the noise level in the original HDF-N image was added back in (Fig. 11-13 panels c). The simulated 5-hr JWST image with the oval PSF was then deconvolved with the known oval PSF, using the Lucy-Richardson method (Lucy 1974), which is shown in Fig. 11-13 (panels d). The images in panels (a) have the round PSF we want, the images in panels (c) is what we will get with an oval JWST PSF, and images in panels (d) is what one may get after careful deconvolution with the oval PSF. The difference between both simulated JWST images in the bottom panels (c–d) and the original image (a) shows significant loss in detail, and object characteristics $(m, r_e, b/a)$ cannot be accurately recovered, in particular for the fainter (lower S/N) objects.

[1] 84 realizations of the same model galaxy as characterized by profile type, magnitude, and effective radius, modeled at different position angles and sub-pixel center positions, times 10 inclination angles (axial ratios b/a).

4. Conclusions

(1) Axis ratios measured with the oval JWST are heavily biased, especially for faint objects (fig. 9–14). In particular:

(1.a) Faint known stars and other known point sources in the original image are no longer round in the simulated JWST images, even after deconvolution. Most remain significantly oval even after deconvolution.

(1.b) Faint objects that were NS-extended in the original image are now mostly round in the JWST images with the oval EW-PSF.

(1.c) The PA's values measured with the oval JWST are especially poor (Fig. 14).

These effects combined are disastrous for studies of structure, morphology, and gravitational lensing, especially because most objects at z>>6–10 are thought to be gravitationally lensed by foreground matter.

(2) The deconvolved r_e values from the oval JWST are heavily overestimated in general. This is because these faint objects are unduly smeared out by the oval PSF, before and even after deconvolution. This smearing in one direction is mostly unrecoverable by deconvolution for faint objects. These effects will significantly affects studies of fundamental galaxy parameters (such as sizes, masses, etc.), and will likely bias observations aimed at distinguishing between different (theoretical/numerical/semi-analytical) galaxy formation scenarios.

(3) Galaxy types (on the 16-step de Vaucouleurs system) in the deconvolved oval JWST images are significantly biased towards earlier types (even after deconvolution) with respect to the input types from the HDF, which are largely known to be type/Irr/peculiar galaxies. Both were determined with the same Artificial Neural Networks (ANN's) as in our earlier HST papers of Odewahn et al. (1996, 2002), Driver et al. (1995, 1998), and Cohen et al. (2003). This bias towards earlier galaxy types in the deconvolved oval JWST images occurs, because the faint objects are on average more smeared out by the oval PSF, which again is mostly unrecoverable by deconvolution.

(4) The noise in the deconvolved JWST is strongly correlated. This is made worse by the image seams (Fi. 11.a–d), which were deliberately left in from the HDF, since JWST mosaics will have a lot more seams, especially if we choose small SCA's. The S/N in the convolved and deconvolved images therefore may look better than it really is. In actuality, the S/N in the convolved and deconvolved images is worse than in the original image. All pixels in the original image are essentially almost independent.

(5) The dynamic range is worse for an oval JWST PSF, before and even after deconvolution. Contrast on faint objects is lost. This effect looks even worse in brighter galaxies with a lot of visible structure (some examples in Fig. 12–13), somewhat resembling the effects from aberrated WF/PC-1 PSF, although the situation for an oval JWST PSF is not quite that bad.

(6) An oval PSF will also push JWST closer to the natural confusion limit (Windhorst et al. 2003), which is not desirable in deep–ultradeep JWST images (AB-limits $\gtrsim$ 31–32 mag). For this reason, we do not consider convolving the oval JWST PSF with another oval PSF that is its conjugate, so that the effective PSF is

round but ∼2× large than the original PSF. This would also result in an effective image S/N that differs by ∼sqrt(2), leading to the biases already observed in this study.

In conclusion, an oval PSF will lead to an irrecoverable loss of the fine spatial resolution of JWST, especially for the faint objects that are JWST's primary aim. Deconvolution algorithms, therefore, fall in the same category as nuclear weapons — their best use is to make sure they will never have to be used ...

RAJ and RAW acknowledge support from NASA grant NAG5-12460 for the work presented in this report. We thank Steve Odewahn and Matt Mountain for helpful discussions.

REFERENCES

Bertin, E., & Arnouts, S. 1996, A&AS, 117, 393

Condon, J. J. 1997 PASP, 109, 166

Driver, S. P., Windhorst, R. A., Ostrander, E. J., Keel, W. C., Griffiths, R. E., & Ratnatunga, K. U. 1995, ApJL, 449, L023

Driver, S. P., Fernandez-Soto, A., Couch, W. J., Odewahn, S. C., Windhorst, R. A., Phillipps, S., Lanzetta, K., & Yahil, A. 1998, ApJL, 496, L093 (astro-ph/9802092)

Lucy, L.B. 1974, AJ, 79, 745

Odewahn, S. C., Windhorst, R. A., Driver, S. P., & Keel, W. C. 1996, ApJL, 472, L013

Odewahn, S. C., Burstein, D., & Windhorst, R. A. 1997, AJ, 114, 2219–2231 (astro-ph/9709069)

Odewahn, S. C., Cohen, S. H., Windhorst, R. A., & Philip, N. S. 2002, ApJ, 568, 539 (astro-ph/0110275)

Pascarelle, S. M., Windhorst, R. A., Keel, W. C., & Odewahn, S. C. 1996, *Nature*, 383, No. 6595, 45

Rauscher, B.J., Isaacs, J., & Long, K. 2000, STScI-NGST-R-0003A (Baltimore: STScI)

Schwarz, U. J. 1978, A&AS, 65, 345

Wild, J. P. 1970, Australian J. Phys., 23, 113

Windhorst, R. A., van Heerde, G. M., & Katgert, P. 1984, A&AS, 58, 1

Windhorst, R. A., Keel, W. C., & Pascarelle, S. M. 1998, ApJL, 494, L027

Windhorst, R. A., Taylor, V. A., Jansen, R. A., Odewahn, S. C., Chiarenza, C. A., Conselice, C. J., de Grijs, R., de Jong, R. S., MacKenty, J. W., Eskridge, P. B., Frogel, J. A., Gallagher III, J. S., Hibbard, J. E., Matthews, L. D., & O'Connell, R. W. 2002, ApJS, 143, p. 113 (astro-ph/0204398)

Windhorst, R. A., Cohen, S. H., Jansen, R. A., Odewahn, S. C., Driver, S. P., Kawata, D., Gibson, B. K., & Hopkins, A. 2002b, in the Lowell Observatory Workshop on "The Outer Edges of Dwarf Irregular Galaxies", Eds. S. Oey & D. Hunter(E-published in http://www.lowell.edu/Workshops/Lowell02/posters.html and astro-ph/0212246)

Windhorst, R.A., Conselice, C.J., & Petro, L.D. 2003, ApJ, (in prep.); see also http://www.stsci.edu:8084/ngst/science/simulations/

This preprint was prepared with the AAS LaTeX macros v5.0.

Appendix A. Model grids used:

m*	b/a	r_e	A	profile (PA=0..90)
26.50	0.9871	2.089	7x7m	Elliptical
27.00	0.9138	2.630	6x6m	Exponential disk
27.50	0.8197	3.311	8x4m	
28.00	0.7200	4.169		
28.50	0.6182	5.248		
29.00	0.5153	6.607		
29.50	0.4119	8.318		
30.00	0.3081	10.47		
30.50	0.2041			
31.00	0.1000			

Each 8-exposure simulation consists of 84 realizations of the same combination of model parameters, but placed at a different sub-pixel center position and with a different position angle. We also place 7 realizations of the PSF in the central portion of the model image. Figure 1 shows an example of a simulated individual 450 s exposure and of the corresponding combined 1-hour image stack for both a $m_{AB}(2\mu m) = 27.9$ and 30.9 elliptical (de Vaucouleurs profile) galaxy model for the case of the nominal 7 m telescope. Figure 2 shows the same simulations for a 8×4 m elliptical primary.

We use the following IRAF **artdata** package parameters:

```
nxc,i,h,10,1,,"Number of PSF centers per pixel in X"
nyc,i,h,10,1,,"Number of PSF centers per pixel in Y"
nxsub,i,h,20,1,,"Number of pixel subsamples in X"
nysub,i,h,20,1,,"Number of pixel subsamples in Y"
nxgsub,i,h,10,1,,"Number of galaxy pixel subsamples in X"
nygsub,i,h,10,1,,"Number of galaxy pixel subsamples in Y"
dynrange,r,h,1000000.,2.,,"Profile intensity dynamic range"
psfrange,r,h,20.,2.,,"PSF convolution dynamic range"
ranbuf,i,h,0,0,,"Random number buffer size"
```

Example of a script used to execute a single 8×450 s simulation:

```
print ("SIMJWST[7x7m primary;0.0386\"/pix] 7 PSF's + 84 disks with ba=0.3081, r_e=5.248 pix, m*=29.50")
!echo ' $  &  29.500   expdisk    5.248  0.3081   '' > gallis.tem
!echo " 206.75  512.25  29.500" > S_29.50_5.248_0.3081_7x7.lis
!echo " 308.50  512.50  29.500" >> S_29.50_5.248_0.3081_7x7.lis
!echo " 410.50  512.00  29.500" >> S_29.50_5.248_0.3081_7x7.lis
!echo " 512.00  512.00  29.500" >> S_29.50_5.248_0.3081_7x7.lis
!echo " 614.25  512.00  29.500" >> S_29.50_5.248_0.3081_7x7.lis
!echo " 716.25  512.25  29.500" >> S_29.50_5.248_0.3081_7x7.lis
!echo " 818.50  512.25  29.500" >> S_29.50_5.248_0.3081_7x7.lis
!arg -m0 posx.lis gallis.tem '$' > gallis.1
!arg -m1 posy.lis gallis.1 '&' > gallis.2
!arg -m1 posa.lis gallis.2 ''' >> S_29.50_5.248_0.3081_7x7.lis
print ("  Generating galaxy models...")
print ("     CRSPLIT exposure #1... 450 s")
mkobjects ("S_29.50_5.248_0.3081_7x7a", output="", title="S_29.50_5.248_0.3081_7x7a", ncols=1024, nlines=1024,
        header="artdata$stdheader.dat", background=(185.148/450./3.5), objects="S_29.50_5.248_0.3081_7x7.lis",
        xoffset=0., yoffset=0., star="moffat", radius=(0.071898/0.0386), beta=2.5, ar=1.0, pa=0., distance=1.,
        exptime=450., magzero=30., gain=3.5, rdnoise=4.41, poisson=yes, seed=INDEF, comments=yes)
mknoise ("S_29.50_5.248_0.3081_7x7a", output="", title="", ncols=1024, nlines=1024, background=0., poisson=no,
        seed=INDEF, ncosrays=5300., energy=60000., radius=0.25, ar=1.0, pa=0.0)
print ("     CRSPLIT exposure #2... 450 s")
mkobjects ("S_29.50_5.248_0.3081_7x7b", output="", title="S_29.50_5.248_0.3081_7x7b", ncols=1024, nlines=1024,
```

```
        header="artdata$stdheader.dat", background=(185.148/450./3.5), objects="S_29.50_5.248_0.3081_7x7.lis",
        xoffset=0., yoffset=0., star="moffat", radius=(0.071898/0.0386), beta=2.5, ar=1.0, pa=0., distance=1.,
        exptime=450., magzero=30., gain=3.5, rdnoise=4.41, poisson=yes, seed=INDEF, comments=yes)
mknoise ("S_29.50_5.248_0.3081_7x7b", output="", title="", ncols=1024, nlines=1024, background=0., poisson=no,
        seed=INDEF, ncosrays=5300., energy=60000., radius=0.25, ar=1.0, pa=0.0)
print ("     CRSPLIT exposure #3... 450 s")
mkobjects ("S_29.50_5.248_0.3081_7x7c", output="", title="S_29.50_5.248_0.3081_7x7c", ncols=1024, nlines=1024,
        header="artdata$stdheader.dat", background=(185.148/450./3.5), objects="S_29.50_5.248_0.3081_7x7.lis",
        xoffset=0., yoffset=0., star="moffat", radius=(0.071898/0.0386), beta=2.5, ar=1.0, pa=0., distance=1.,
        exptime=450., magzero=30., gain=3.5, rdnoise=4.41, poisson=yes, seed=INDEF, comments=yes)
mknoise ("S_29.50_5.248_0.3081_7x7c", output="", title="", ncols=1024, nlines=1024, background=0., poisson=no,
        seed=INDEF, ncosrays=5300., energy=60000., radius=0.25, ar=1.0, pa=0.0)
print ("     CRSPLIT exposure #4... 450 s")
mkobjects ("S_29.50_5.248_0.3081_7x7d", output="", title="S_29.50_5.248_0.3081_7x7d", ncols=1024, nlines=1024,
        header="artdata$stdheader.dat", background=(185.148/450./3.5), objects="S_29.50_5.248_0.3081_7x7.lis",
        xoffset=0., yoffset=0., star="moffat", radius=(0.071898/0.0386), beta=2.5, ar=1.0, pa=0., distance=1.,
        exptime=450., magzero=30., gain=3.5, rdnoise=4.41, poisson=yes, seed=INDEF, comments=yes)
mknoise ("S_29.50_5.248_0.3081_7x7d", output="", title="", ncols=1024, nlines=1024, background=0., poisson=no,
        seed=INDEF, ncosrays=5300., energy=60000., radius=0.25, ar=1.0, pa=0.0)
print ("     CRSPLIT exposure #5... 450 s")
mkobjects ("S_29.50_5.248_0.3081_7x7e", output="", title="S_29.50_5.248_0.3081_7x7e", ncols=1024, nlines=1024,
        header="artdata$stdheader.dat", background=(185.148/450./3.5), objects="S_29.50_5.248_0.3081_7x7.lis",
        xoffset=0., yoffset=0., star="moffat", radius=(0.071898/0.0386), beta=2.5, ar=1.0, pa=0., distance=1.,
        exptime=450., magzero=30., gain=3.5, rdnoise=4.41, poisson=yes, seed=INDEF, comments=yes)
mknoise ("S_29.50_5.248_0.3081_7x7e", output="", title="", ncols=1024, nlines=1024, background=0., poisson=no,
        seed=INDEF, ncosrays=5300., energy=60000., radius=0.25, ar=1.0, pa=0.0)
print ("     CRSPLIT exposure #6... 450 s")
mkobjects ("S_29.50_5.248_0.3081_7x7f", output="", title="S_29.50_5.248_0.3081_7x7f", ncols=1024, nlines=1024,
        header="artdata$stdheader.dat", background=(185.148/450./3.5), objects="S_29.50_5.248_0.3081_7x7.lis",
        xoffset=0., yoffset=0., star="moffat", radius=(0.071898/0.0386), beta=2.5, ar=1.0, pa=0., distance=1.,
        exptime=450., magzero=30., gain=3.5, rdnoise=4.41, poisson=yes, seed=INDEF, comments=yes)
mknoise ("S_29.50_5.248_0.3081_7x7f", output="", title="", ncols=1024, nlines=1024, background=0., poisson=no,
        seed=INDEF, ncosrays=5300., energy=60000., radius=0.25, ar=1.0, pa=0.0)
print ("     CRSPLIT exposure #7... 450 s")
mkobjects ("S_29.50_5.248_0.3081_7x7g", output="", title="S_29.50_5.248_0.3081_7x7g", ncols=1024, nlines=1024,
        header="artdata$stdheader.dat", background=(185.148/450./3.5), objects="S_29.50_5.248_0.3081_7x7.lis",
        xoffset=0., yoffset=0., star="moffat", radius=(0.071898/0.0386), beta=2.5, ar=1.0, pa=0., distance=1.,
        exptime=450., magzero=30., gain=3.5, rdnoise=4.41, poisson=yes, seed=INDEF, comments=yes)
mknoise ("S_29.50_5.248_0.3081_7x7g", output="", title="", ncols=1024, nlines=1024, background=0., poisson=no,
        seed=INDEF, ncosrays=5300., energy=60000., radius=0.25, ar=1.0, pa=0.0)
print ("     CRSPLIT exposure #8... 450 s")
mkobjects ("S_29.50_5.248_0.3081_7x7h", output="", title="S_29.50_5.248_0.3081_7x7h", ncols=1024, nlines=1024,
        header="artdata$stdheader.dat", background=(185.148/450./3.5), objects="S_29.50_5.248_0.3081_7x7.lis",
        xoffset=0., yoffset=0., star="moffat", radius=(0.071898/0.0386), beta=2.5, ar=1.0, pa=0., distance=1.,
        exptime=450., magzero=30., gain=3.5, rdnoise=4.41, poisson=yes, seed=INDEF, comments=yes)
mknoise ("S_29.50_5.248_0.3081_7x7h", output="", title="", ncols=1024, nlines=1024, background=0., poisson=no,
        seed=INDEF, ncosrays=5300., energy=60000., radius=0.25, ar=1.0, pa=0.0)
print ("  Stack the 8 CRSPLITs for an equivalent 1 hour exposure...")
imcombine ("S_29.50_5.248_0.3081_7x7?.fits", "S_29.50_5.248_0.3081_7x7", rejmask="", plfile="", sigma="",
        logfile="", combine="average", reject="crreject", project=no, outtype="real", offsets="none",
        masktype="none", maskvalue=0., blank=0., scale="none", zero="none", weight="none", statsec="[*,*]",
        expname="exptime", lthreshold=INDEF, hthreshold=INDEF, mclip=yes, lsigma=3., hsigma=3.,
        rdnoise="4.41", gain="3.5", snoise="0.01", sigscale=0.1, pclip=-0.5, grow=1.)
print ("  Displaying image...")
xdisplay ("S_29.50_5.248_0.3081_7x7.fits", buffer=1, z1=5., z2=500.)
print ("  Performing QPHOT aperture photometry...")
qphot ("S_29.50_5.248_0.3081_7x7.fits", 3., 10., 5., "11.", coords="posxy.lis", output="default",
        zmag=30., exposure="exptime", epadu=3.5, interactive=no, verbose=no)
```

```
txdump ("S_29.50_5.248_0.3081_7x7.fits.mag.1", "id,xcenter,ycenter,msky,area,flux,mag,merr,perror",
        yes, headers=yes, parameters=no, > "tmp")
!echo "# ID  x_cen   y_cen  skyDN areaPIX   fluxDN   mag  e_mag   perror" > S_29.50_5.248_0.3081_7x7.pht
!tail +5 tmp | \
        awk '{printf("%3d %7.2f %7.2f %6.2f %7.2f %9.2f %6.3f %5.3f %8s\n",$1,$2,$3,$4,$5,$6,$7,$8,$9)}' \
        >> S_29.50_5.248_0.3081_7x7.pht
print ("  Performing SExtractor object extraction/measurement...")
!sex S_29.50_5.248_0.3081_7x7.fits -assoc_name posxy.lis -catalog_name S_29.50_5.248_0.3081_7x7.sex
delete ("gallis.*,*mag.1,tmp", yes, verify=no)
print (" ")
```

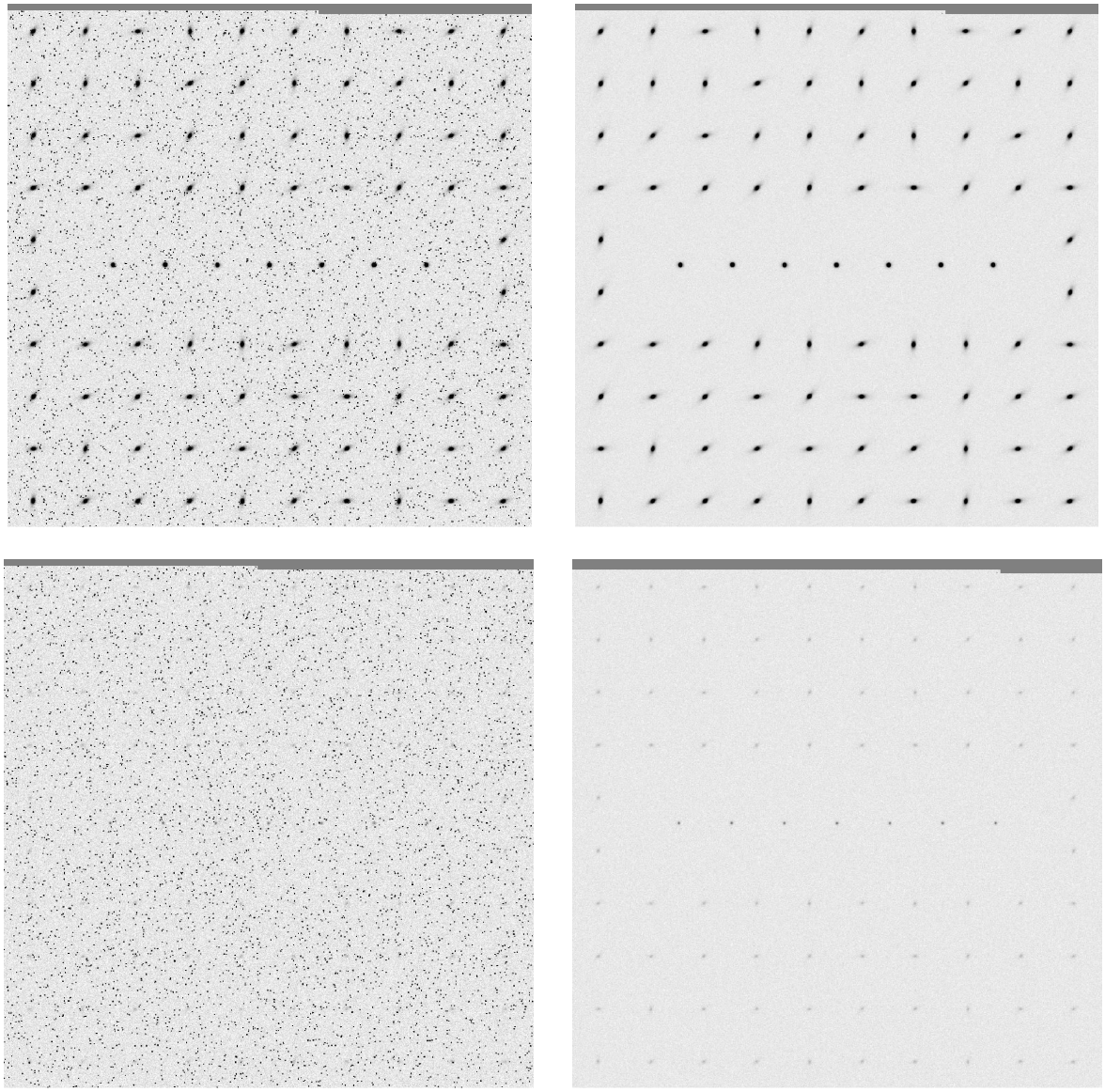

Fig. 1.— Example of four simulated frames for galaxies with de Vaucouleurs light-profiles for the case of a 7 m diameter round primary. The central seven objects in each frame are point sources, the brightest unsaturated one which was used as PSF. *(a)* Single simulated 450 s exposure of a set of $m_{AB}(2\mu m) = 27.93$ galaxies, each having an effective radius of $5.248 \times 0\farcs0386 = 0\farcs206$ and axis ratio $b/a = 0.308$. *(b)* A stack of 8 such exposures (equivalent to a 3600 s exposure) combined using a cosmic ray rejection algorithm. *(c)* As *(a)*, but for $m_{AB}(2\mu m) = 30.93$ galaxies. *(d)* As *(b)*, but for $m_{AB}(2\mu m) = 30.93$ galaxies.

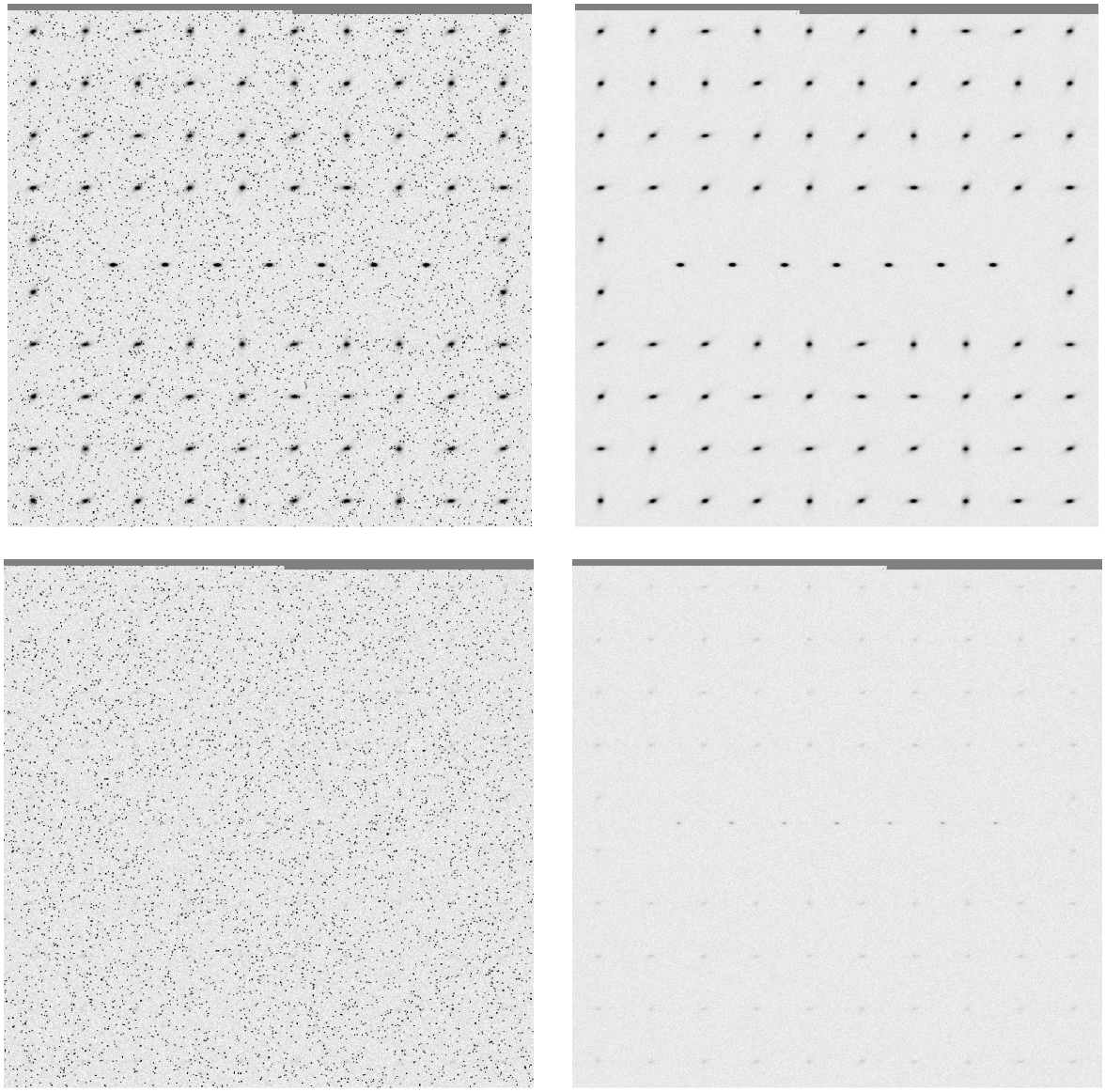

Fig. 2.— As Fig. 1 for the case of an elliptical primary with major and minor axis diameters of 8 and 4 m. The pixel size is assumed to be the same as for a 7 m diameter round mirror in order not to undersample the PSF along the image axis corresponding to the 8 m aperture axis. Note the clear oval character of the central seven PSF stars, and the generally more biased PA-values when compared to Fig. 1.

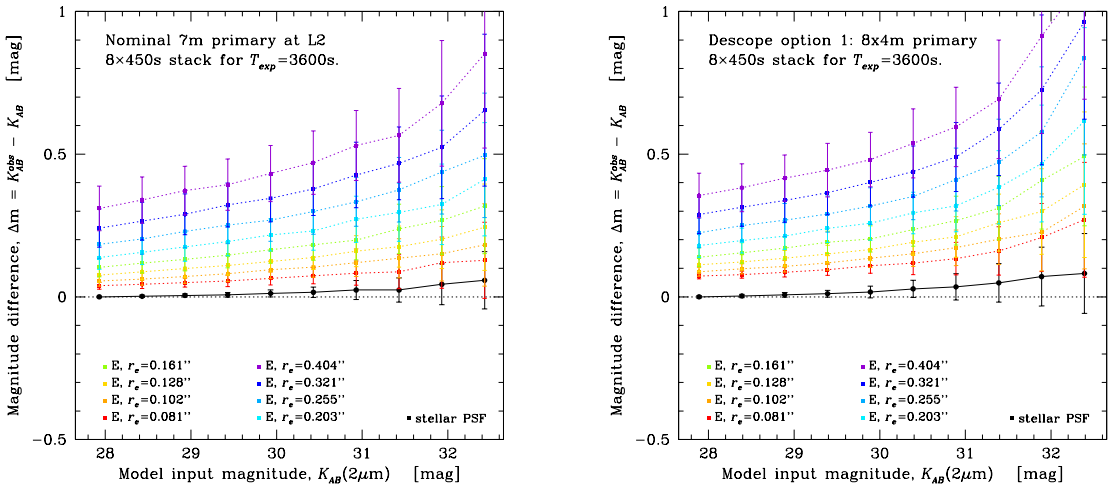

Fig. 3.— (*left*) Comparison of the model input magnitudes for the de Vaucouleurs light-profiles. K_{AB} -band magnitudes were recovered from the simulated exposure stack for the nominal 7 m telescope using SExtractor (Bertin & Arnouts 1996). Measurements are shown as a function of magnitude, K_{AB}, and model effective (half-light) radius, r_e. Each data point represents the median of hundreds of simulated galaxy models (typically 840, but fewer at the faintest magnitudes where some model objects were no longer detected by SExtractor). The quartile range of the individual measurements is indicated by the error bars, which are centered on each sample median. For a given fixed object magnitude, progressively more flux becomes irretrievably lost in the noise as the object signal is spread over a larger solid angle (because their surface brightness gets lower). As r_e becomes larger, the probability of detecting a single object photon in an 8×450 s exposure becomes much less than 1 in a progressively large number of "object pixels". If the galaxy profile can be resolved and its characteristic shape recovered well enough to recognize it as being a de Vaucouleurs rather than an exponential profile, an appropriate correction for lost flux may be made. (*right*) The same case, but for an elliptical primary with major and minor axis diameters of 8 and 4 m. The flux loss is more pronounced for the oval PSF than for the nominal telescope, even at comparable S/N, and the recovery of the characteristic profile shape is hindered by the reduced resolution along one of the image axes.

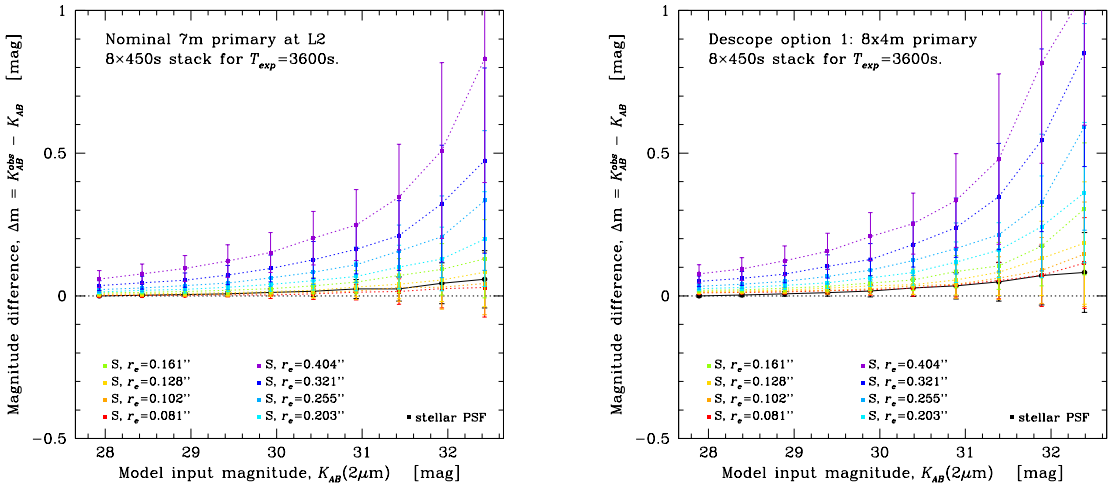

Fig. 4.— As Fig. 3, but now for exponential disk models. Note as in Fig. 3.a–b, that the flux loss for the oval PSF is more pronounced than for the nominal telescope, even at comparable S/N, and the recovery of the characteristic profile shape is hindered by the reduced resolution along one of the image axes.

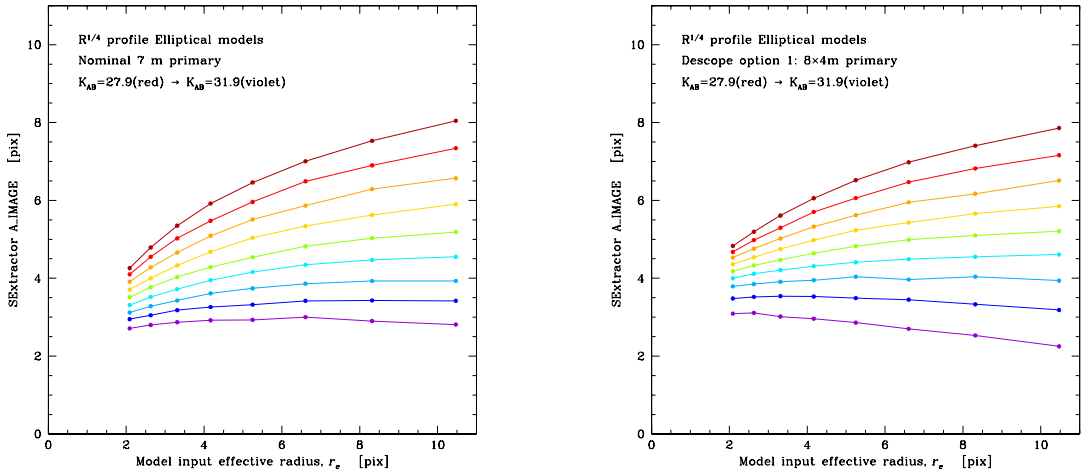

Fig. 5.— SExtractor major axis diameter A_IMAG versus model input effective radius, r_e, for de Vaucouleurs profile models for the nominal 7 m telescope (*left*) and for a 8×4 m primary (*right*). Points and curves are color coded according to the model input magnitude (27.50–31.50 mag) and represent the median of the individual measurements. The A_IMAG parameter is not identical to the r_e parameter, but it is far more easily measured in bulk with SExtractor than the r_e parameter with the interacting MORPHO package (Odewahn et al. 1996), and so it is plotted here, even though this results in relations with slope unequal to 45deg. Nonetheless, the relations are monotonic for AB$\lesssim$30.5–31.0 mag for the nominal telescope, and for AB$\lesssim$30.0 mag for the oval PSF.

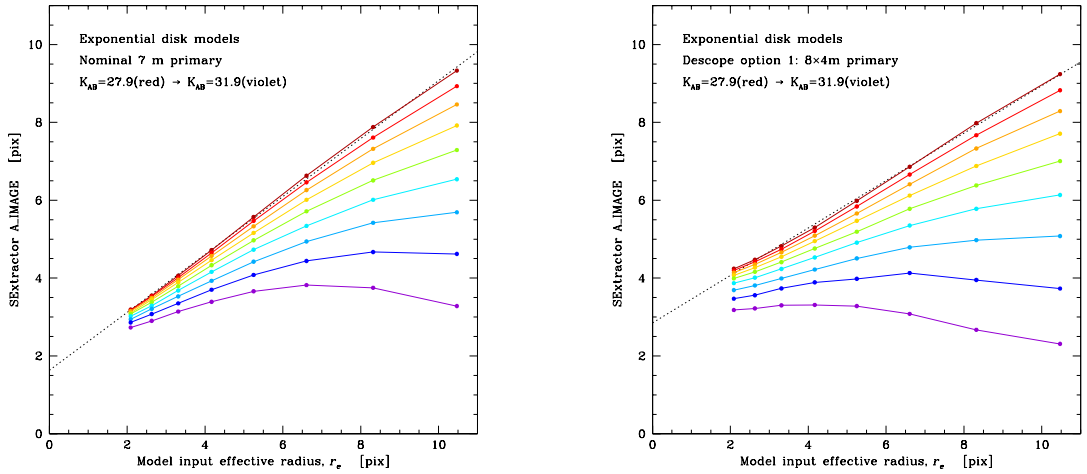

Fig. 6.— As Fig. 5 but for exponential disk models. Again, the relations are monotonic for AB $\lesssim$ 30.5 mag for the nominal telescope, and for AB $\lesssim$ 29.5–30.0 mag for the oval PSF, resulting in a loss of the measurability of the half-light radius in the faintest magnitude bin for the oval PSF.

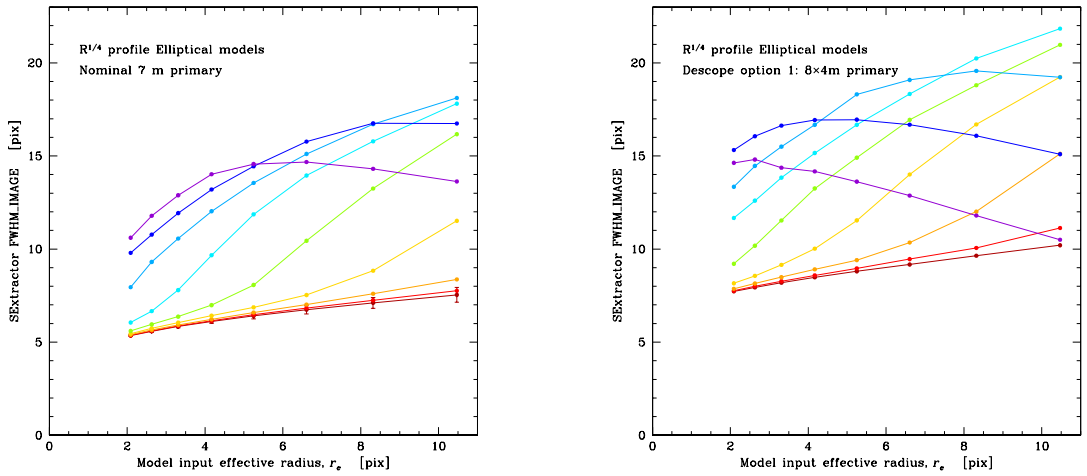

Fig. 7.— SExtractor FWHM versus model input effective radius, r_e, for de Vaucouleurs profile models for the nominal 7 m telescope (*left*) and for a 8×4 m primary (*right*). Points and curves are color-coded as in Fig. 5. The SExtractor FWHM parameter is not identical to the r_e parameter, but it is far more easily measured in bulk with SExtractor than the r_e parameter with the interacting MORPHO package (Odewahn et al. 1996), and so it is plotted here, even though this results in relations with slope unequal to 45deg. Nonetheless, the relations are monotonic for AB $\lesssim$ 30.5 mag for the nominal telescope, and for AB $\lesssim$ 30.0 mag for the oval PSF.

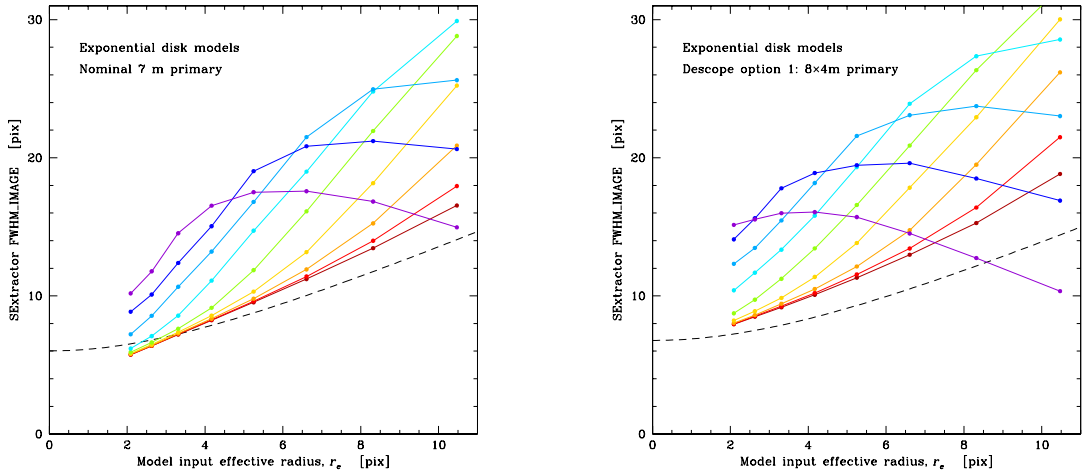

Fig. 8.— As Fig. 7 but for exponential disk models. Again, the relations are monotonic for AB $\lesssim$ 30.5 mag for the nominal telescope, and for AB $\lesssim$ 29.5–30.0 mag for the oval PSF, resulting in a loss of the measurability of the half-light radius in the faintest magnitude bin for the oval PSF.

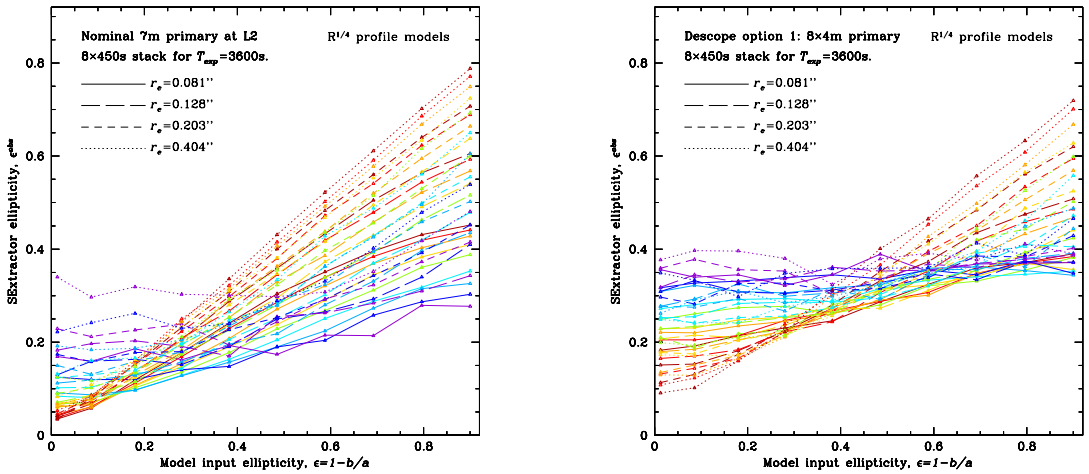

Fig. 9.— Measured ellipticity versus model input ellipticity, for de Vaucouleurs profile models for the nominal 7 m telescope (*left*) and for a 8×4 m primary (*right*). Points and curves are color-coded according to model input magnitude from $K_{AB} = 27.9$ (red) to $K_{AB} = 31.9$ (violet blue) as in Fig. 5. The line styles code four different model input effective radii. How well the ellipticities are recovered is a strong function of both magnitude and effective radius. In short, except for the faintest magnitude bin, the nominal telescope results in monotonic relations between output and input axis ratio, while this is no longer true for the faintest 3–4 magnitude bins and for all axis ratios $b/a \lesssim 0.4$ in th case of the oval PSF. Hence, there is a significant loss of the measurability of axis ratios in the faintest magnitude 2–3 bin and the roundest galaxies in case of the oval PSF.

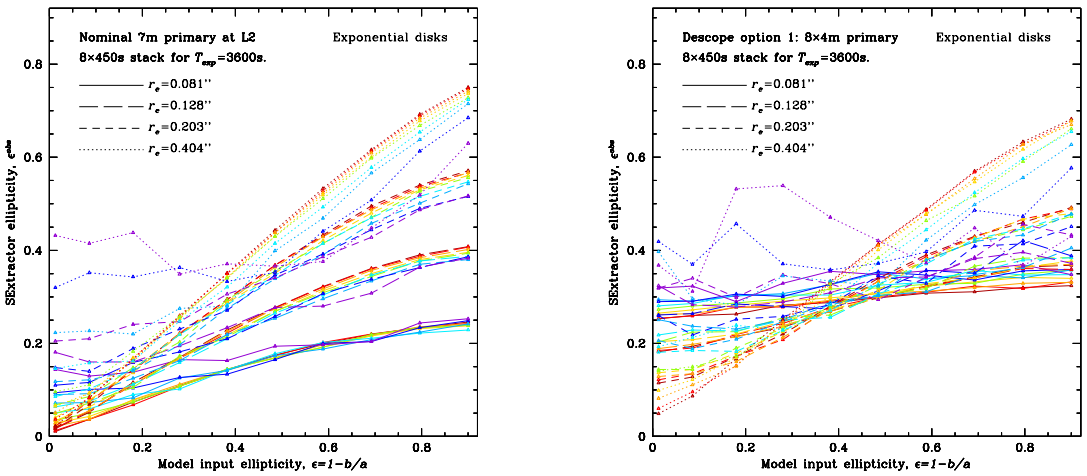

Fig. 10.— As Fig. 9 but for exponential disk models. (These simulations were done for a more limited grid, given the stringent time deadline for this report, and given that each set of simulation generated several 100 Gbytes of disk-space). Again, except for the faintest magnitude bin, the nominal telescope results in monotonic relations between output and input axis ratio, while this is no longer true for the faintest 3–4 magnitude bins and for all axis ratios $b/a \lesssim 0.4$ in th case of the oval PSF. Hence, there is a significant loss of the measurability of axis ratios in the faintest magnitude 2–3 bin and the roundest galaxies in case of the oval PSF.

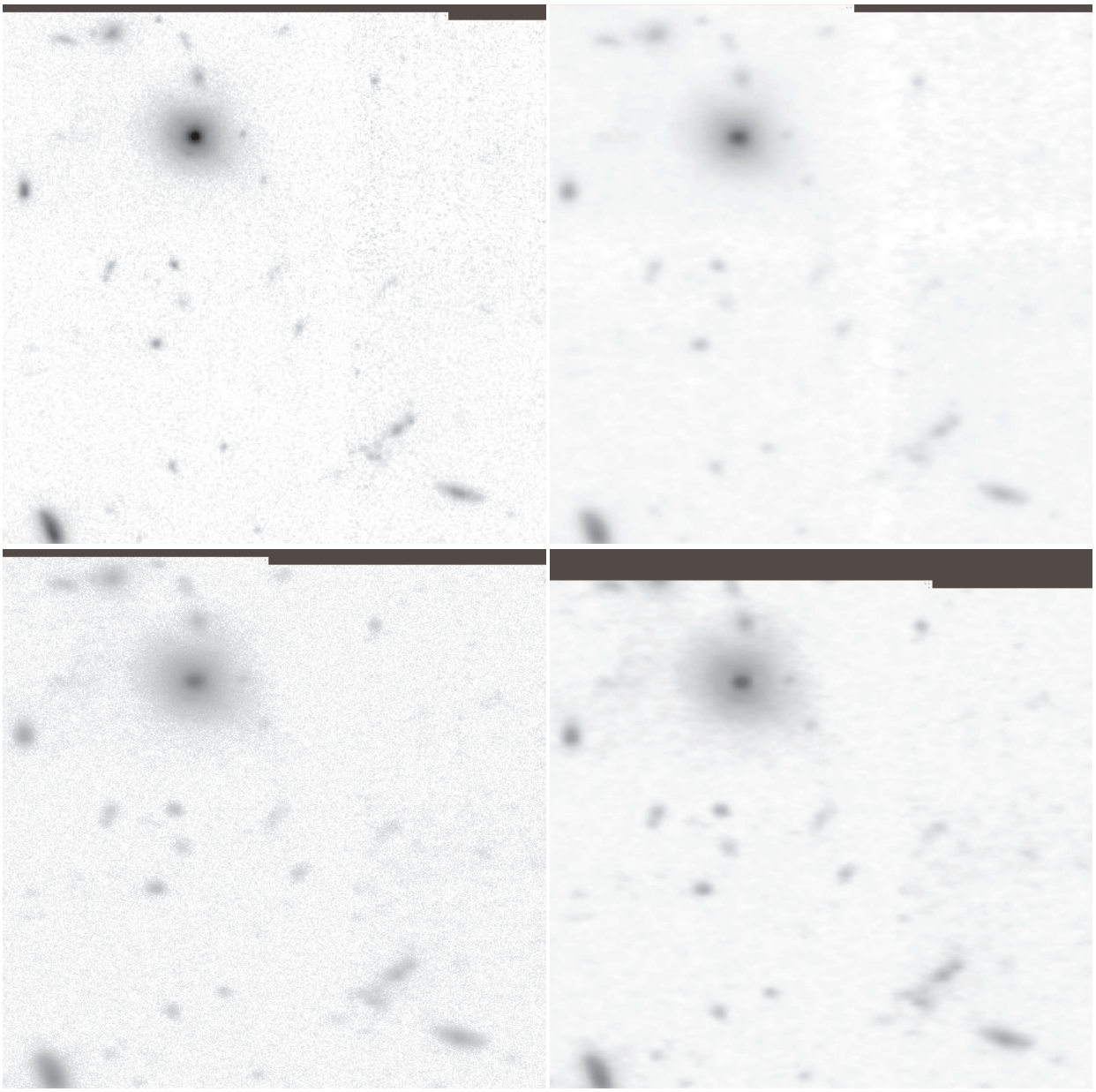

Fig. 11.— *Comparison of the real HDF-N F814W images with a round PSF and the simulated JWST images from an oval 8×4 meter mirror.* **(a)** [**Upper Left**] Original 50-orbit HDF-N F814W image, which is representative for a 5-hr J–K band image with a 7-meter JWST with a round PSF (ignoring effects from the rest-frame wavelength or morphological K-correction, which are to first order small over the sampled redshift range of interest; Windhorst et al. 2002). **(b)** [**Upper Right**] Simulated 5-hr JWST image with oval PSF for a descoped JWST mirror of assumed size 8x4 meters. This image was obtained by convolving (a) with the appropriate elliptical PSF, which in this case is clearly East-West extended. **(c)** [**Lower Left**] Simulated 5-hr JWST image with the oval PSF of panel (b), but with same noise as the original HDF-N image added back in, since convolution with oval PSF smooths the noise. **(d)** [**Lower Right**] Simulated 5-hr JWST image with oval PSF (from panel c), but deconvolved with the known oval PSF. The images in (a) have the round PSF we want, the images in (c) is what we will get with an oval JWST PSF, and images in (d) is what one may get after careful deconvolution with the oval PSF. The difference between both simulated JWST images in the bottom panels (c–d) and the original image (a) shows significant loss in detail, and object characteristics $(m, r_e, b/a)$ cannot be accurately recovered, in particular for the fainter (lower S/N) objects.

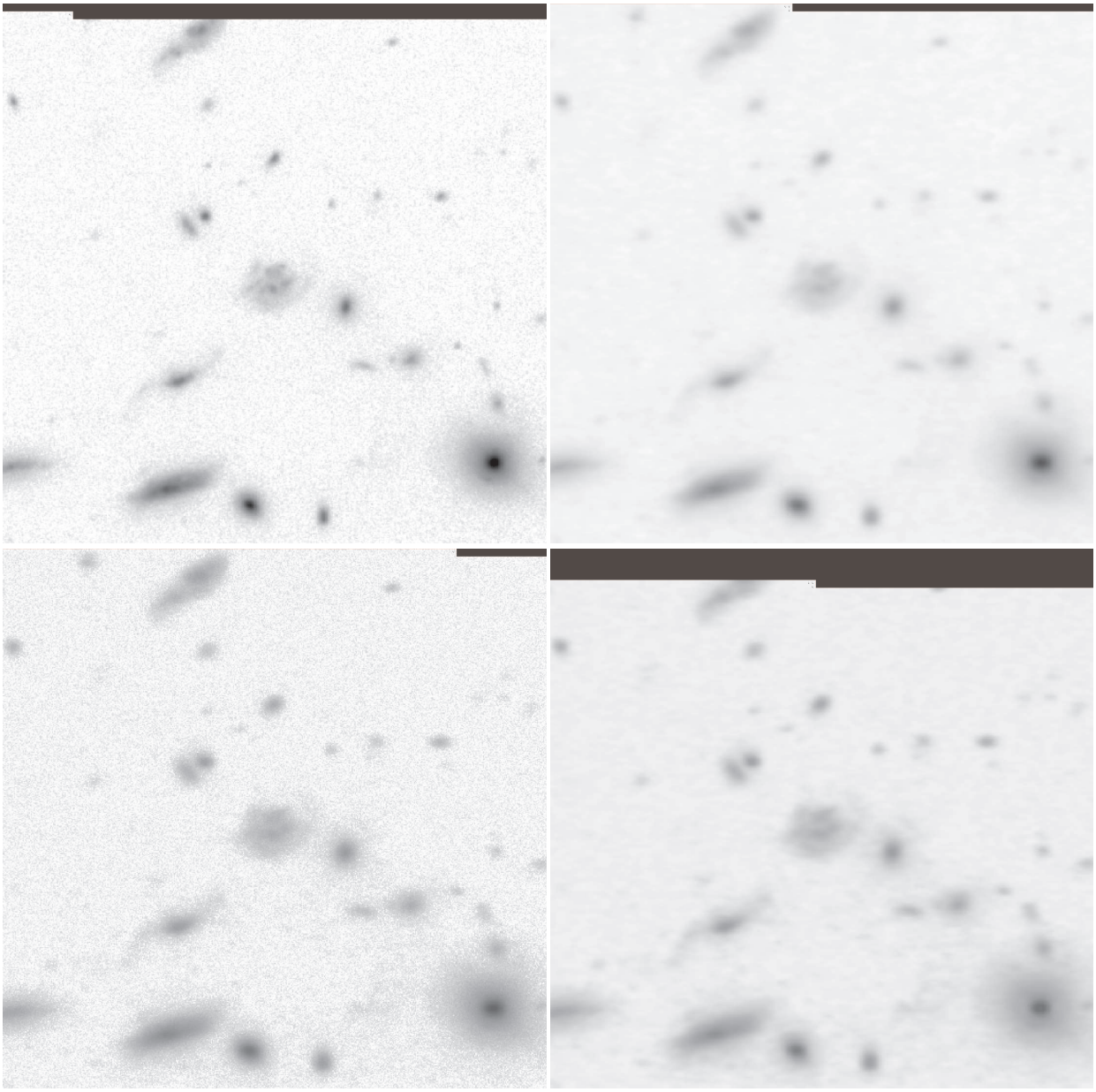

Fig. 12.— *Comparison of the real HDF-N F814W images with a round PSF and the simulated JWST images from an oval 8×4 meter mirror.* Same as Fig. 11.a–d, but for a region in CCD WF2 of the HDF-N. Note the loss of detail in the structure of resolved galaxies, in addition to the effects mentioned in Fig. 11.

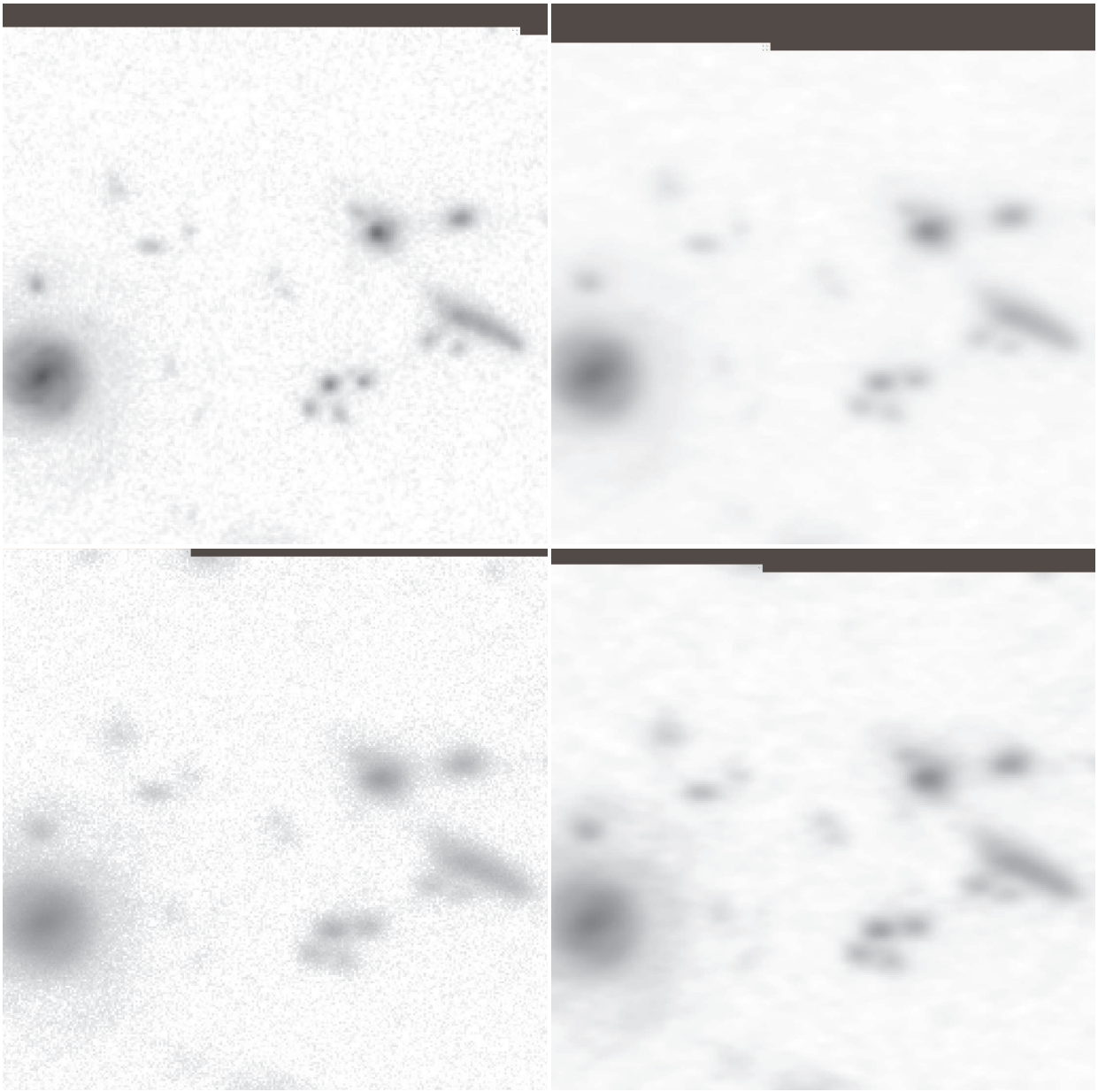

Fig. 13.— *Comparison of the real HDF-N F814W images with a round PSF and the simulated JWST images from an oval 8×4 meter mirror.* Same as Fig. 11.a–d and 12.a–d, but for a enlarged region in CCD WF4 of the HDF-N. Note the decreased ability to resolve faint and nearly unresolved objects, in addition to the effects mentioned in Fig. 11.

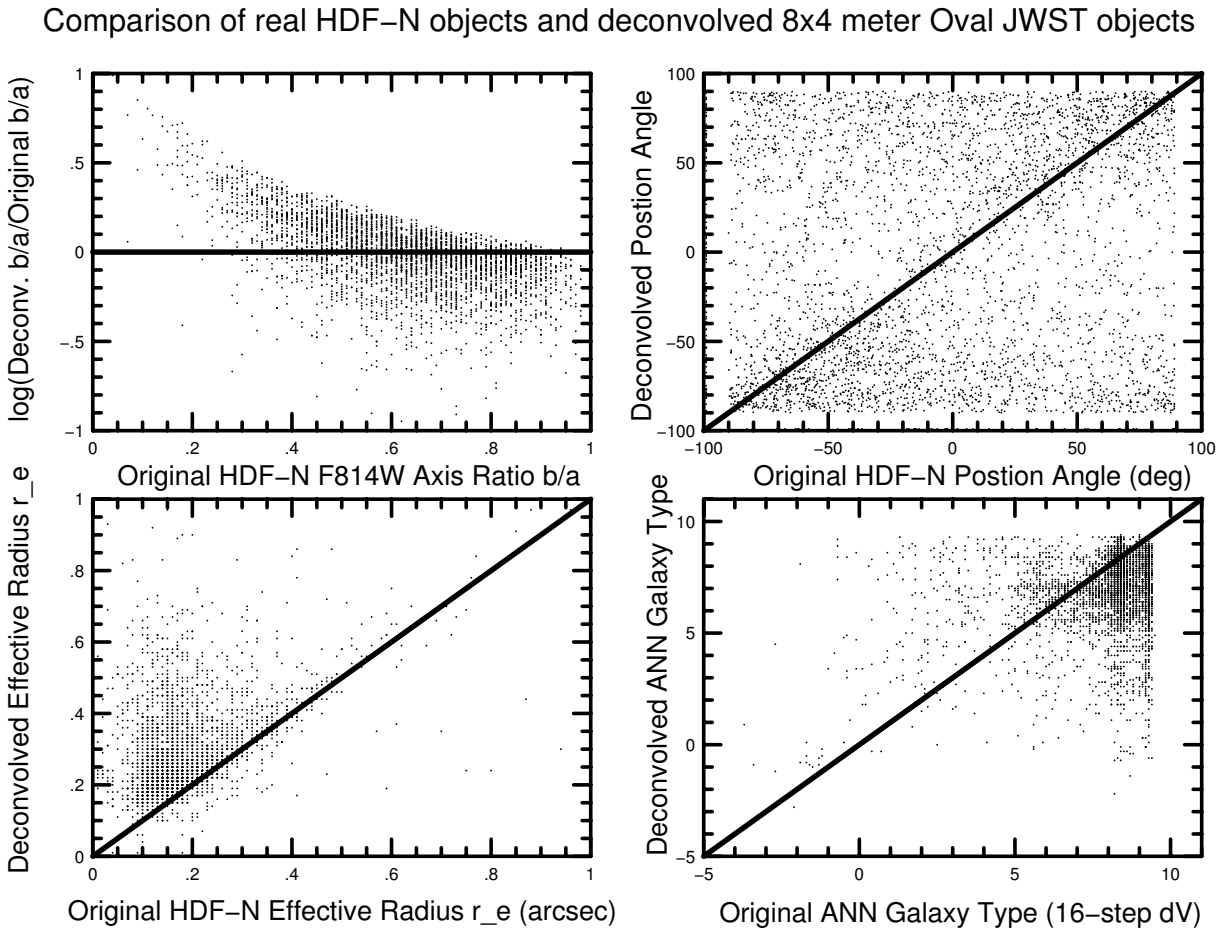

Fig. 14.— **(a)** [**Upper Left**] the deconvolved/original vs original Axis Ratio b/a — Axis ratios for the oval JWST are heavily biased, especially for faint objects. This is disastrous for the studies of structure, morphology, and gravitational lensing, especially because most objects at z>>6–10 are thought to be gravitationally lensed by foreground matter. **(b)** [**Upper Right**] Deconvolved vs. Original Position Angle. The reproduction of PA's is especially poor for the oval JWST, with the same deleterious results for structure, morphology, and lensing studies as in panel (a). **(c)** [**Lower Left**] Deconvolved vs. Original effective radius. The deconvolved r_e values from the oval JWST are heavily overestimated in general. This is because these faint objects are unduly smeared out by the oval PSF, which is largely not recoverable by deconvolution. **(d)** [**Lower Right**] The deconvolved JWST vs. original Galaxy types on the 16-step de Vaucouleurs system, made with the same Artificial Neural Networks (ANN's) as in the HST papers of Odewahn et al. (1996, 2002), Driver et al. (1995, 1998), and Cohen et al. (2003). The input types from the HDF which are largely known to be type/Irr/peculiar galaxies are significantly biased towards earlier types in the oval JWST images, even after deconvolution, since objects are more smeared out.